International Journal of
Science, Architecture, Technology and Environment

Fixed-Wing versus Multirotor UAV Recognition from Radar Track Kinematics Using a Jump-Markov Multiple-Model Estimator

Bui Tien Anh[1]*

[1]*Missile Faculty, Air Defence-Air Force Academy, Ha Noi, Viet Nam*

**Corresponding author: buitienanh@lqdtu.edu.vn*

DOI: https://doi.org/10.63680/ijsate112637.31

Abstract

Recognising whether a small unmanned aerial vehicle (UAV) is of fixed-wing or multirotor type is a prerequisite for threat assessment and countermeasure selection in counter-UAS surveillance, yet many deployed surveillance radars provide only plot-level kinematics without micro-Doppler signatures. Falileev and Shatovkin (2020) proposed recognising the UAV type from track kinematics alone, exploiting the fact that only rotary-wing platforms can hover for a sustained period: a three-mode jump-Markov system (manoeuvre, non-manoeuvre, hover) is estimated with a second-order generalised pseudo-Bayesian (GPB2) filter, and a rotary-wing declaration is issued when the hover mode is estimated on *n* consecutive scans within the same azimuth sector.

This paper restates that algorithm in a reproducible form, analyses its transition probability matrices (TPMs), and evaluates it by Monte Carlo simulation over 1,300 synthetic radar tracks at a 3 s update period.

We show that the published TPMs are not row-stochastic and, once normalised, have identical rows, i.e. they describe a memoryless mode process that cannot accumulate evidence over scans. In our simulations the published parameterisation never declared a multirotor (0/600 tracks, measurement noise 1–25 m). Replacing the TPM with a diagonally dominant, persistence-aware matrix yields 100% recognition of multirotors at every noise level with a median latency of 9–12 s after hover onset and at most 1% false declarations on nominal fixed-wing tracks, against a median latency of 6–63 s for a filtered speed-threshold baseline. For low-airspeed fixed-wing aircraft flying into strong headwinds, a horizontal-velocity gate on the mode-conditioned estimate reduces false declarations from 38% to 8% (3-of-3 rule) at a cost of 3 s median latency. We discuss the latency–false-alarm trade-off governed by *n* and the fundamental limits of kinematics-only recognition.

Keywords: *unmanned aerial vehicle; target recognition; jump-Markov system; multiple-model estimation; GPB2; hover detection; counter-UAS; radar tracking.*

1. Introduction

Small unmanned aerial vehicles (UAVs) have become ubiquitous in civil and military airspace, and their misuse has motivated a large body of work on detection, tracking and classification for counter-unmanned aircraft systems (C-UAS) [1]–[3]. Detection of small UAVs by radar, radio-frequency, acoustic and electro-optical sensors is well covered in the literature, whereas the subsequent task of recognising the *type* of a detected UAV has received comparatively less attention [4]. Knowing whether a target is a fixed-wing aircraft or a multirotor (helicopter-type) platform is operationally valuable: the two classes differ in endurance, speed, payload, typical missions and the most effective countermeasures.

Most radar-based UAV classifiers rely on micro-Doppler signatures generated by rotating propellers and rotors [5]–[7]. These approaches require coherent dwell times and waveform access that many legacy or low-cost surveillance radars do not offer; such radars output only plots (range, azimuth, elevation) at the antenna revisit rate, typically 1–5 s. Algorithms developed for recognising manned aircraft from track data are poorly suited to small UAVs because of the very different flight envelopes [8]. Falileev and Shatovkin [8] therefore proposed a recognition algorithm that uses only *trajectory features*. Its key physical premise is simple: a fixed-wing aircraft cannot hover for an extended period, while a multirotor routinely does. Both classes, however, perform manoeuvring and non-manoeuvring flight, so the trajectory is modelled as a stochastic system with random, jump-like changes of structure [9], [10] with three modes—manoeuvre,

non-manoeuvre and hover—and the mode sequence is estimated by a multiple-model filter. A rotary-wing declaration is issued when the hover mode is estimated on three consecutive scans within the same azimuth sector.

The original paper demonstrated the idea on one recorded trajectory of each class but did not report Monte Carlo statistics, sensitivity to sensor accuracy, or the latency–false-alarm trade-off of the decision rule. In attempting to reproduce the method we found that the published transition probability matrices (TPMs) require interpretation and, once interpreted consistently, prevent the hover mode from ever being selected under realistic radar noise. The contributions of this paper are therefore:

(1) A self-contained, reproducible restatement of the Falileev–Shatovkin algorithm as a GPB2 estimator for a three-mode jump-Markov linear system, together with explicit mode-conditioned dynamic models (Section 3).

(2) An analysis of the published TPMs showing that they are not row-stochastic and, after normalisation, are memoryless (identical rows), which removes the temporal evidence accumulation on which hover detection depends (Section 4).

(3) A persistence-aware TPM and an optional velocity gate that restore the intended behaviour, and a Monte Carlo evaluation over 1,300 synthetic tracks comparing the published parameterisation, the modified algorithm and a filtered speed-threshold baseline across measurement noise levels and *n*-of-*n* decision rules (Sections 5–6).

Section 7 discusses limitations—in particular that all results are obtained on synthetic trajectories—and Section 8 concludes.

2. Related Work

Radar-based UAV classification. Surveys of machine-learning-based drone detection and classification [4] and of detection, tracking and interdiction of amateur drones [3] show that micro-Doppler features dominate radar-based classification. Molchanov et al. [5] classified small UAVs and birds from micro-Doppler signatures, and Mendis et al. [6] applied deep learning to Doppler radar spectrograms; the physics of micro-Doppler is described by Chen [7]. These methods require coherent processing that is not always available, which motivates kinematics-only approaches such as [8].

Multiple-model estimation. Systems with Markovian switching structure were studied in the Russian literature as systems with random jump-like structure [9], [10], and in the Western literature through the generalised pseudo-Bayesian (GPB) estimators originating with Ackerson and Fu [11] and the interacting multiple model (IMM) algorithm of Blom and Bar-Shalom [12]. Comprehensive treatments are given in [13]–[15]. The GPB2 estimator maintains one filter per pair of consecutive modes (M^2 filters for M modes) and merges hypotheses after each update; it is the structure implied by equations (1)–(11) of [8]. In multiple-model trackers the TPM is a design parameter that encodes the expected sojourn time in each mode; its diagonal is usually chosen from the mean sojourn time τ and scan period T as $p_{ii} \approx 1 - T/\tau$ [13], [15]. This design principle is central to Section 4.

Dynamic models. The constant-velocity (CV) model driven by white acceleration noise and the Singer model [16] are standard choices for non-manoeuvring and manoeuvring flight respectively; a survey of dynamic models is given by Li and Jilkov [14].

3. Problem Formulation and Algorithm

3.1. Jump-Markov model of UAV flight

Let the target state be $\mathbf{x}_k = [x, y, z, \dot{x}, \dot{y}, \dot{z}]^T$ in a local Cartesian frame centred on the radar, observed every $T = 3$ s. The flight regime is a discrete Markov chain $s_k \in \{1, 2, 3\}$, where $s_k = 1$ denotes manoeuvre, $s_k = 2$ non-manoeuvring flight and $s_k = 3$ hover, with transition probabilities $\mu(s_{k+1} \mid s_k)$. Conditioned on the mode, the state and measurement evolve as

$$x_{k+1} = \Phi(s_{k+1})\, x_k + w_k(s_{k+1}), \quad w_k \sim N(0, Q(s_{k+1})), \tag{1}$$

$$z_k = H\, x_k + v_k, \quad v_k \sim N(0, R), \quad H = [I_3 \;\; 0_3], \tag{2}$$

where $\mathbf{z}_k$ is the radar plot converted to Cartesian coordinates. Modes 1 and 2 use a CV model with transition matrix $\Phi_{CV} = [[I_3,\ TI_3],[0,\ I_3]]$ and discretised white-acceleration noise of standard deviation $\sigma_a = 4$ m/s² (horizontal) and 2 m/s² (vertical) for manoeuvre, and 0.3 m/s² and 0.15 m/s² for non-manoeuvre. The hover model holds the position and resets the velocity:

$$\Phi(3) = [[I_3, 0],[0, 0]], \quad Q(3) = \mathrm{diag}(0.5^2, 0.5^2, 0.25^2, 0.1^2, 0.1^2, 0.05^2), \tag{3}$$

so that a hovering platform is described by a position random walk of about 0.5 m per scan and a near-zero velocity. The original paper does not give explicit model matrices; equation (3) is our concrete realisation of its hover structure.

3.2. GPB2 estimator

At scan k the estimator holds, for each mode s_k, a mode-conditioned estimate $\hat{x}(s_k)$, its covariance $\hat{P}(s_k)$ and the mode probability $p(s_k)$. For every mode pair (s_k, s_{k+1}) a Kalman filter step is performed [8], [13]:

$$\tilde{x}(s_k,s_{k+1}) = \Phi(s_{k+1})\, \hat{x}(s_k), \quad \tilde{P}(s_k,s_{k+1}) = \Phi(s_{k+1})\, \hat{P}(s_k)\, \Phi^T(s_{k+1}) + Q(s_{k+1}), \tag{4}$$

$$\nu = z_{k+1} - H\, \tilde{x}, \quad V = H\, \tilde{P}\, H^T + R, \quad K = \tilde{P}\, H^T V^{-1}, \tag{5}$$

$$\hat{x}(s_k,s_{k+1}) = \tilde{x} + K\,\nu, \quad \hat{P}(s_k,s_{k+1}) = (I - K\,H)\,\tilde{P}, \tag{6}$$

with the Gaussian likelihood of each hypothesis

$$\Lambda(s_k,s_{k+1}) = |2\pi V|^{-1/2} \exp\{ -\tfrac{1}{2}\, \nu^{T} V^{-1} \nu \}. \tag{7}$$

The unnormalised joint weights $\omega(s_k, s_{k+1}) = \mu(s_{k+1} \mid s_k)\, \Lambda(s_k, s_{k+1})\, p(s_k)$ give the updated mode probabilities and the merged mode-conditioned estimates:

$$p(s_{k+1}) = \Sigma_{s_k}\, \omega(s_k,s_{k+1}) \,/\, \Sigma_{s_{k+1}} \Sigma_{s_k}\, \omega(s_k,s_{k+1}), \tag{8}$$

$$\hat{x}(s_{k+1}) = \Sigma_{s_k}\, \bar{\omega}(s_k|s_{k+1})\, \hat{x}(s_k,s_{k+1}), \tag{9}$$

$$\hat{P}(s_{k+1}) = \Sigma_{s_k}\, \bar{\omega}(s_k|s_{k+1})\, [\, \hat{P}(s_k,s_{k+1}) + \Delta\, \Delta^{T}\,], \quad \Delta = \hat{x}(s_k,s_{k+1}) - \hat{x}(s_{k+1}), \tag{10}$$

where $\bar{\omega}(s_k \mid s_{k+1}) = \omega(s_k, s_{k+1}) \,/\, \Sigma_{s_k}\, \omega(s_k, s_{k+1})$. The structure estimate is the maximum a posteriori mode

$$\hat{s}_{k+1} = \arg\max_s\, p(s_{k+1} = s). \tag{11}$$

Equations (4)–(11) are equivalent to equations (1)–(11) of [8]; the per-scan cost is $M^2 = 9$ Kalman updates of a six-dimensional state, which our unoptimised Python implementation executes in about 0.4 ms.

3.3. Decision rule

Let N_k denote the index of the azimuth sector containing plot $\mathbf{z}_k$ (we use sectors of 1°). Following [8], the type decision is an *n*-of-*n* rule: the UAV is declared rotary-wing at the first scan *k* for which

$$\hat{s}_{k-n+1} = \ldots = \hat{s}_k = 3 \quad \text{and} \quad N_{k-n+1} = \ldots = N_k, \tag{12}$$

and fixed-wing otherwise. The declaration is latched: once rotary-wing parameters are adopted they are used for all subsequent scans. The original algorithm starts with fixed-wing TPM values and switches to rotary-wing values after the declaration; the original authors recommend $n = 3$ for $T = 3$ s. Fig. 1 shows the resulting logic, including the optional velocity gate introduced in Section 4.3.

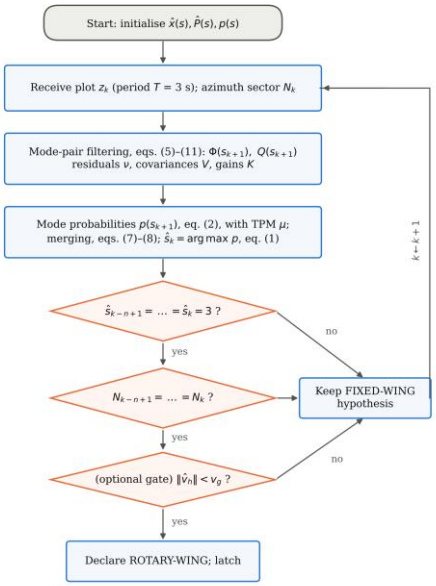


Figure 1. Logic of the recognition algorithm (redrawn and extended from [8]). The velocity gate (Section 4.3) is optional; without it the scheme coincides with the original algorithm.

4. Analysis of the Transition Probability Matrices

4.1. Normalisation of the published values

Reference [8] specifies, for each UAV type, the marginal frequencies of the three modes obtained from typical trajectories and a set of conditional probabilities $\mu(s_{k+1} \mid s_k)$. Arranged as a matrix with rows indexed by s_k and columns by s_{k+1}, the published values do not sum to one along either dimension (e.g. 0.08 + 0.25 + 0.005 = 0.335 for the fixed-wing row s_k = 1). Normalising each row reproduces the stated marginal frequencies (0.24/0.75/0.01 for fixed-wing and 0.42/0.42/0.16 for rotary-wing) to within rounding, which strongly suggests that row normalisation is the intended interpretation. Table 1 lists both forms.

Table 1. Transition probabilities $\mu(s_{k+1} = j \mid s_k = i)$ of [8]: published values and row-normalised values used in this study.

Type / row i	Published (j = 1, 2, 3)	Row-normalised (j = 1, 2, 3)
Fixed-wing, i = 1	0.08, 0.25, 0.005	0.239, 0.746, 0.015
Fixed-wing, i = 2	0.08, 0.25, 0.005	0.239, 0.746, 0.015
Fixed-wing, i = 3	0.08, 0.25, 0	0.242, 0.758, 0
Rotary-wing, i = 1	0.14, 0.14, 0.05	0.424, 0.424, 0.152
Rotary-wing, i = 2	0.14, 0.14, 0.06	0.412, 0.412, 0.176
Rotary-wing, i = 3	0.14, 0.14, 0.05	0.424, 0.424, 0.152

4.2. Memorylessness and its consequence

Every normalised matrix in Table 1 has (almost) identical rows, $\mu(j \mid i) \approx \pi_j$. Substituting into (8) gives

$$p(s_{k+1} = j) \propto \pi_j \, \Sigma_i \, \Lambda(i, j) \, p(s_k = i), \tag{13}$$

so the prior probability of entering mode j is the same whatever the previous mode was. The chain has no persistence: its expected sojourn time in any mode is $1/(1 - \pi_j)$ scans, e.g. 1.02 scans (3 s) for hover in the fixed-wing matrix and 1.2 scans for hover in the rotary-wing matrix. Evidence for hover must then be re-established from scratch at every scan, and the only way the hover mode can win (11) is if a *single-scan* likelihood ratio $\Lambda(\cdot,3)/\Lambda(\cdot,2)$ exceeds $\pi_2/\pi_3 \approx 50$ (fixed-wing values) or ≈ 2.8 (rotary-wing values).

The single-scan likelihoods of hover and non-manoeuvre are, however, nearly equal for a hovering target. Once the non-manoeuvre filter has converged its velocity estimate is close to zero, so both modes predict essentially the same position; with radar noise of several metres the innovation covariance V is dominated by R and the ratio stays close to one. Hover can therefore be distinguished from slow straight flight only by accumulating evidence over several scans, which a memoryless TPM forbids. The 3-of-3 rule in (12) cannot compensate for this, because it requires $\hat{s}_k = 3$ on each scan individually.

4.3. Persistence-aware TPM and velocity gate

We replace the published matrices by a single diagonally dominant TPM designed from mean sojourn times, as is standard for multiple-model trackers [13], [15]:

$$\mu_P = [[0.85, 0.10, 0.05], [0.05, 0.90, 0.05], [0.03, 0.07, 0.90]], \tag{14}$$

corresponding to mean sojourn times of 20 s, 30 s and 30 s for manoeuvre, non-manoeuvre and hover at T = 3 s. The same matrix is used before and after the declaration, because type information is carried by the n-of-n rule rather than by the prior. The resulting algorithm is denoted **B**; the published (normalised) parameterisation is **A**.

Kinematics alone cannot distinguish a hovering multirotor from a fixed-wing aircraft whose *ground* speed is near zero, which happens when a slow aircraft flies into a strong headwind. To reduce false declarations in this case we optionally require the horizontal speed of the non-manoeuvre-conditioned estimate $\hat{x}(s = 2)$ to be below a threshold v_g:

$$\|\hat{v}_h(s_k = 2)\| < v_g, \quad v_g = 2 \text{ m/s}, \tag{15}$$

on each of the n scans. This variant is denoted **D**. As a reference we also implement a baseline **C** that is common in practice: a single CV Kalman filter (σ_a = 1 m/s²) whose estimated horizontal speed must stay below 2.5 m/s on n consecutive scans in the same azimuth sector.

5. Simulation Setup

Because recorded radar tracks of both classes with ground-truth flight regimes were not available to us, all experiments use synthetic trajectories generated at 10 Hz and sampled at the radar scan period. The generator and estimator code are described below in enough detail to be re-implemented; the parameters are summarised in Table 2.

Fixed-wing (nominal). Airspeed 18–32 m/s, constant wind 0–10 m/s with first-order gusts (time constant 5 s, intensity 1.5 m/s/√s), alternating straight legs (20–90 s) and coordinated turns of 4–12 °/s (10–45 s), random vertical rate (σ = 1 m/s).

Fixed-wing (stress). As above, but airspeed 15–19 m/s and wind 10–15 m/s, so that the ground speed occasionally approaches zero when flying upwind (ground speed below 2.5 m/s on 1.1% of scans).

Multirotor. Alternating cruise legs at 4–14 m/s (20–80 s) and hover periods of 20–90 s with station-keeping jitter ($\sigma \approx 0.6$ m/s) and bounded acceleration of 4 m/s². Ground-truth regime labels are hover when the platform is in station-keeping and its horizontal speed is below 1.5 m/s, manoeuvre when acceleration exceeds 0.5 m/s², and non-manoeuvre otherwise.

Each track lasts 600 s (200 scans) and starts at a range of 3–7 km and altitude of 150–600 m. Radar plots are perturbed by independent Gaussian Cartesian noise with horizontal standard deviation $\sigma \in \{1, 3, 5, 10, 15, 25\}$ m and

vertical standard deviation 1.3σ. For each σ, 100 fixed-wing and 100 multirotor tracks are simulated; 100 stress-case fixed-wing tracks are added at σ = 10 m, giving 1,300 tracks in total. Recognition latency is measured from the first hover onset in the ground truth (median onset 45 s after track initiation).

Table 2. Simulation and algorithm parameters.

Parameter	Value
Scan period T	3 s
Track duration / scans	600 s / 200
Horizontal noise σ (vertical 1.3σ)	1, 3, 5, 10, 15, 25 m
Monte Carlo runs per class and σ	100
σ_a manoeuvre / non-manoeuvre (horiz.)	4.0 / 0.3 m/s²
Hover model Q(3)	see eq. (3)
Azimuth sector width	1°
Decision rule	n-of-n, n = 2…6 (default 3)
Velocity gate v_g (D) / baseline threshold (C)	2.0 / 2.5 m/s
Initial mode probabilities	(0, 1, 0)

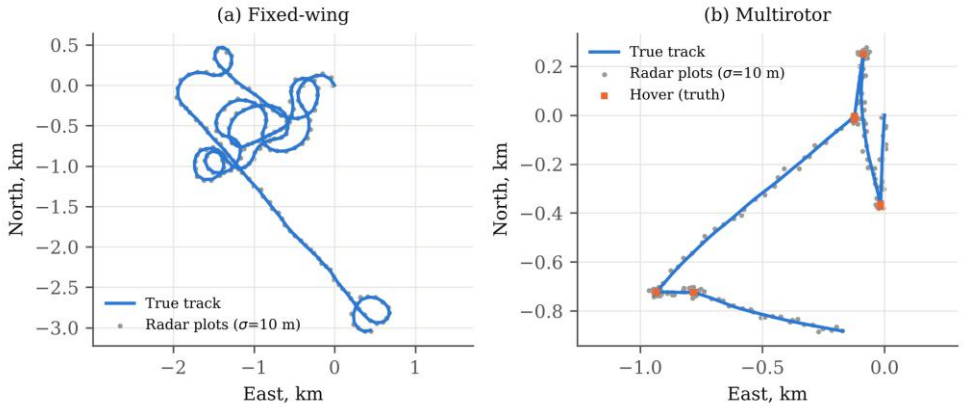


Figure 2. Examples of synthetic trajectories (plan view, relative to the track start) with radar plots at σ = 10 m: (a) nominal fixed-wing track; (b) multirotor track with ground-truth hover periods marked.

6. Results

6.1. Illustrative run

Fig. 3 shows the true and estimated regimes for the multirotor track of Fig. 2(b) at σ = 10 m. With the published TPM (algorithm A) the estimate alternates between non-manoeuvre and manoeuvre and never selects hover, even during 75 s of continuous hovering. With the persistence-aware TPM (algorithm B) the hover periods are recovered with short delays, and the rotary-wing declaration is issued at t = 54 s, i.e. 9 s after the first hover onset. Fig. 4 compares the posterior hover probability $p(s_k = 3)$ under algorithm B for this multirotor and for the fixed-wing track of Fig. 2(a): for the fixed-wing aircraft it remains near the prior level throughout the flight and no declaration is issued.

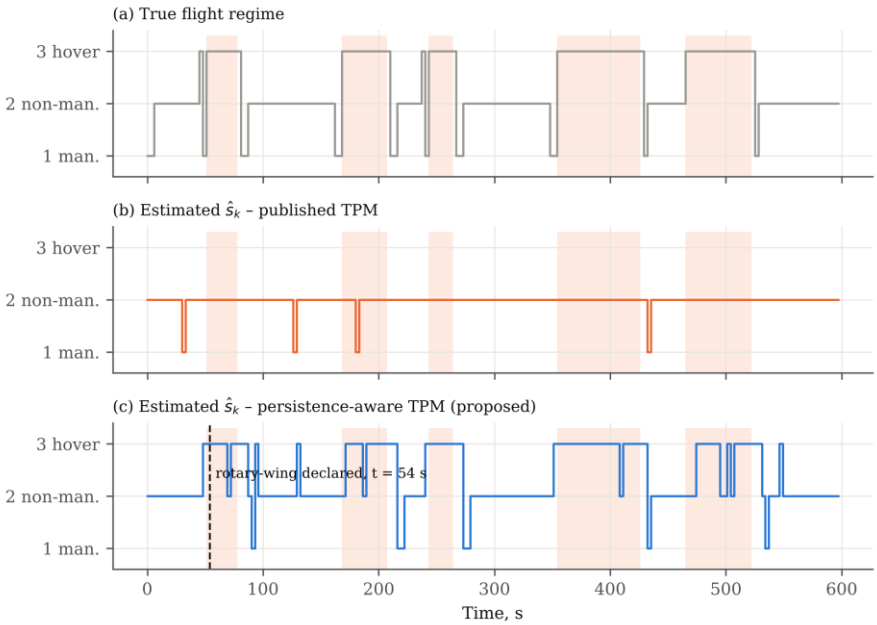


Figure 3. Flight regime of a multirotor track (σ = 10 m): (a) ground truth; (b) estimate with the published, row-normalised TPM; (c) estimate with the persistence-aware TPM. Shaded bands mark true hover; the dashed line marks the 3-of-3 rotary-wing declaration.

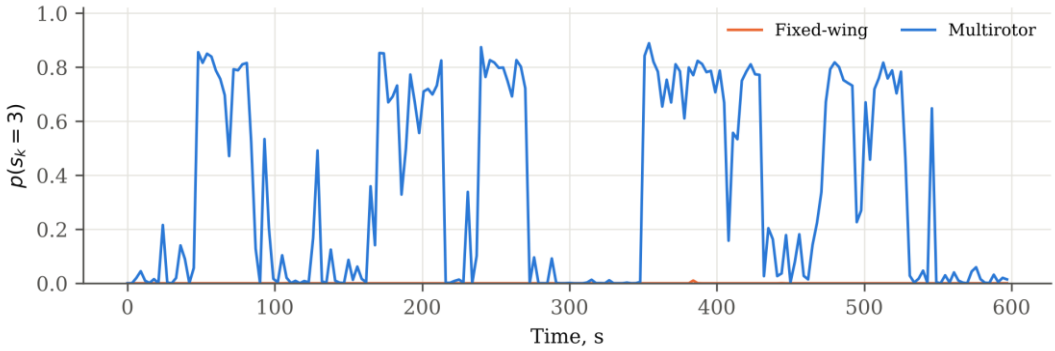


Figure 4. Posterior hover probability under algorithm B for the fixed-wing and multirotor tracks

6.2. Effect of measurement noise

Table 3 reports, for the 3-of-3 rule, the probability of correctly recognising a multirotor (P_D), the probability of falsely declaring a nominal fixed-wing aircraft rotary-wing (P_{FA}), and the median latency after hover onset. Algorithm A did not declare a single multirotor at any noise level (0 of 600 tracks); it also produced no false alarms, so in effect it reports every target as fixed-wing. We also tried the rotary-wing matrix of Table 1 from the first scan (50 tracks at σ = 10 m) with the same outcome, confirming that the failure is caused by memorylessness rather than by the fixed-wing prior. Algorithms B and D recognised all multirotors at all noise levels. False declarations on nominal fixed-wing tracks were 0–1%.

Table 3. Recognition performance versus horizontal measurement noise (3-of-3 rule, 100 tracks per class and σ). Entries: P_D (%) / P_{FA} (%) / median latency after hover onset (s).

σ, m	A (published)	B (proposed)	D (B + gate)	C (baseline)
1	0 / 0	100 / 0 / 9	100 / 0 / 9	100 / 0 / 6
3	0 / 0	100 / 0 / 9	100 / 0 / 9	100 / 0 / 9
5	0 / 0	100 / 0 / 9	100 / 0 / 9	100 / 0 / 12
10	0 / 0	100 / 0 / 9	100 / 0 / 12	100 / 0 / 25.5
15	0 / 0	100 / 1 / 9	100 / 0 / 13.5	100 / 0 / 33
25	0 / 0	100 / 1 / 12	100 / 0 / 21	97 / 0 / 63

Fig. 5 plots the median latency. The latency of algorithm B is essentially independent of σ up to 15 m (9 s, i.e. the minimum three scans) and grows to 12 s at 25 m. The baseline C is slightly faster at σ = 1 m but degrades quickly as noise

increases, because its velocity estimate must be smoothed heavily to stay under the threshold: median latency rises to 25.5 s at 10 m and 63 s at 25 m, its 90th-percentile latency exceeds 300 s at σ = 25 m, and 3% of multirotors are missed. The velocity gate in D adds 0–9 s of median latency relative to B.

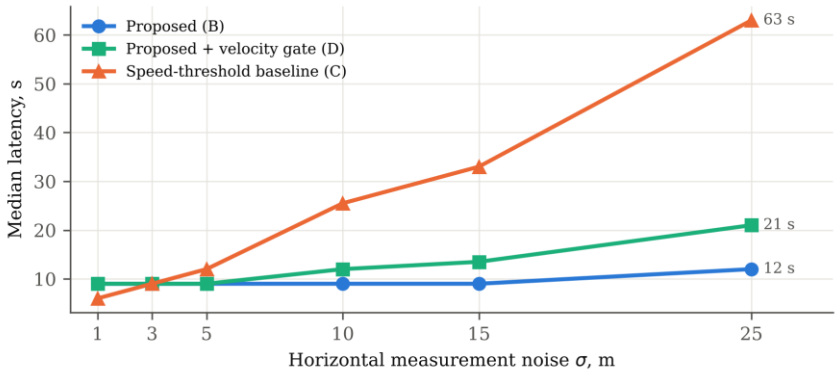


Figure 5. Median recognition latency after hover onset versus horizontal measurement noise

6.3. Choice of n and low-speed fixed-wing aircraft

Table 4 and Fig. 6 examine the *n*-of-*n* rule at σ = 10 m, now including the stress case of slow fixed-wing aircraft in strong wind. For nominal tracks no algorithm produced false declarations for any *n*. The stress case is much harder: with *n* = 3, algorithm B falsely declares 38% of these aircraft, because their ground speed upwind is low enough to be explained by the hover model within the noise. The velocity gate reduces this to 8% (D) while keeping the 12 s median latency; the baseline reaches 4% but with a 25.5 s median latency. Increasing *n* trades latency for robustness: D with *n* = 5 gives 3% false declarations at 18 s median latency, a better operating point than any configuration of C, which needs *n* ≥ 4 (60 s or more) to reach comparable false-declaration rates and starts missing multirotors at *n* ≥ 5.

Table 4. Effect of *n* at σ = 10 m. P_{FA} is given for nominal and stress-case fixed-wing tracks; latencies are after hover onset.

n	Alg.	P_D, %	P_{FA} nominal, %	P_{FA} stress, %	Median lat., s	90th pct., s
2	B	100	0	68	3	12
	D	100	0	31	6	12
	C	100	0	12	9	30.3
3	B	100	0	38	9	21
	D	100	0	8	12	21
	C	100	0	4	25.5	127.2
4	B	100	0	12	12	42.9
	D	100	0	5	15	42.9
	C	99	0	1	60	224.4
5	B	100	0	5	15	93.6
	D	100	0	3	18	96.6
	C	92	0	1	102	337.5
6	B	100	0	2	19.5	105
	D	100	0	2	24	105
	C	72	0	0	175.5	442.5

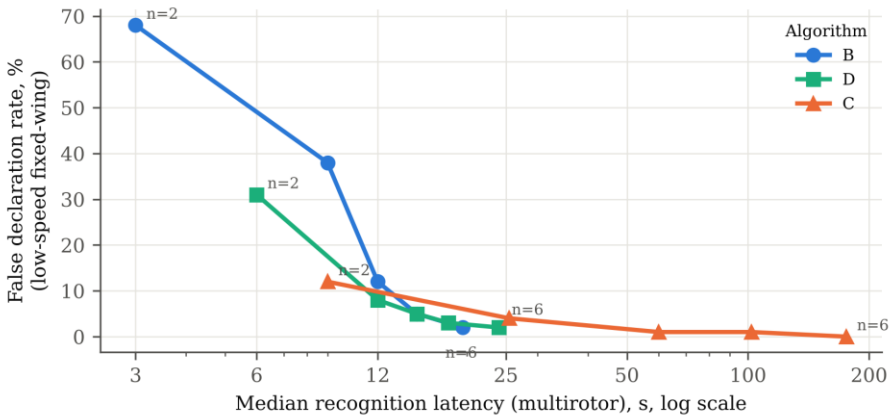


Figure 6. Trade-off between multirotor recognition latency and false declarations on low-speed fixed-wing aircraft at σ = 10 m, as *n* varies from 2 to 6 (end points labelled).

6.4. Accuracy of regime estimation

Although the type decision is the main output, the regime estimate itself is useful for tracking and intent assessment. Over all multirotor scans, the fraction of scans on which the hover/non-hover status was estimated correctly was 53.5%, 52.5% and 52.0% for algorithm A at σ = 1, 10 and 25 m—equal to the share of non-hover scans, consistent with A never selecting hover—and 94.2%, 89.3% and 83.6% for algorithm B. Table 5 gives the hover/non-hover confusion matrix of B at σ = 10 m: 91.8% of true hover scans are recognised, while 13.0% of non-hover scans are labelled hover, mostly at the start and end of hover periods when the platform decelerates or accelerates slowly.

Table 5. Hover/non-hover confusion matrix of algorithm B on multirotor tracks (σ = 10 m, 19,800 scans).

True \ estimated	Hover	Not hover	Total
Hover	8,605 (91.8%)	765 (8.2%)	9,370
Not hover	1,356 (13.0%)	9,074 (87.0%)	10,430

7. Discussion

Why the published configuration fails here but appeared to work in [8]. The trajectories in [8] were plotted in geocentric coordinates of order 10^6 m and appear to originate from navigation logs rather than from a surveillance radar; with metre-level noise the single-scan likelihood ratio can be larger than in our radar-noise setting. Even so, at σ = 1 m algorithm A did not select hover in our simulations, so the results of [8] probably also depend on model matrices that were not published. Our point is not that the original concept is wrong—the persistence-aware variant confirms that hover persistence is a strong and robust discriminant—but that the TPM must encode mode persistence for the concept to work with radar data.

Role of the TPM. In multiple-model filtering the TPM is often regarded as a secondary tuning parameter. For mode *recognition* it is primary: it determines how much evidence is integrated over time. The identical-row structure of the published matrices is a natural outcome of estimating mode frequencies from typical trajectories; the transition structure should instead be estimated from the sequence of regimes, or designed from sojourn times as in (14).

Limits of kinematics-only recognition. The stress case shows the physical limit: a fixed-wing aircraft holding near-zero ground speed is kinematically indistinguishable from a hovering multirotor over a short window. Gating on the velocity estimate and lengthening the window reduce but cannot eliminate such errors. Where available, fusing the kinematic decision with micro-Doppler [5]–[7], radar cross-section fluctuation or RF features would resolve these cases. Conversely, a multirotor that never hovers—e.g. one flying a pre-programmed transit route—will be reported as fixed-wing by any hover-based method; the declaration should therefore be understood as "hover-capable" rather than as a complete type classification.

Limitations of this study. All results are obtained on synthetic trajectories with Cartesian Gaussian noise, a single target per track, perfect plot-to-track association and no birds or clutter. The azimuth-sector condition was implemented with 1° sectors; its value relative to the hover mode itself was small in our setting. Validation on recorded radar data with ground-truth flight logs, and comparison with IMM implementations and learned classifiers, are the most important next steps.

8. Conclusion

We restated the trajectory-based UAV type recognition algorithm of Falileev and Shatovkin as a GPB2 estimator for a three-mode jump-Markov system and evaluated it on 1,300 synthetic radar tracks. The published transition probabilities, once normalised, describe a memoryless mode process; in our simulations this prevented hover from being detected, and no multirotor was recognised. A persistence-aware transition matrix restores the intended behaviour: all multirotors were recognised with a median latency of 9–12 s after hover onset for radar noise up to 25 m, with 0–1% false declarations on nominal fixed-wing tracks, outperforming a filtered speed-threshold baseline in latency by a factor of about three to five at $\sigma \geq 10$ m. For slow fixed-wing aircraft in strong headwinds, a velocity gate together with $n = 3–5$ offers a practical compromise between latency and false declarations. These findings support the practical use of hover persistence as a kinematic recognition cue, provided the mode-transition model is designed to accumulate evidence over time.

Acknowledgments

The authors express their sincere appreciation to all individuals and institutions who indirectly contributed to the completion of this research

Declaration of Conflicting Interests

The authors declare that there are no conflicts of interest regarding the research, authorship, or publication of this article.

Funding

The author received no financial support for the research, authorship and publication of this article.

References

[1] I. Guvenc, F. Koohifar, S. Singh, M. L. Sichitiu, and D. Matolak, "Detection, tracking, and interdiction for amateur drones," *IEEE Communications Magazine*, vol. 56, no. 4, pp. 75–81, 2018.
[2] A. I. Godunov, S. V. Shishkov, and N. K. Yurkov, "Complex for detection and counteraction of small-sized unmanned aerial vehicles," *Reliability and Quality of Complex Systems*, no. 2(6), pp. 62–70, 2014 (in Russian).
[3] E. D. Filin and R. V. Kirichek, "Methods for detecting small unmanned aerial vehicles based on analysis of the electromagnetic spectrum," russiandrone.ru, accessed Aug. 2019 (in Russian).
[4] B. Taha and A. Shoufan, "Machine learning-based drone detection and classification: State-of-the-art in research," *IEEE Access*, vol. 7, pp. 138669–138682, 2019.
[5] P. Molchanov, R. I. A. Harmanny, J. J. M. de Wit, K. Egiazarian, and J. Astola, "Classification of small UAVs and birds by micro-Doppler signatures," *International Journal of Microwave and Wireless Technologies*, vol. 6, no. 3–4, pp. 435–444, 2014.
[6] G. J. Mendis, T. Randeny, J. Wei, and A. Madanayake, "Deep learning based Doppler radar for micro UAS detection and classification," in *Proc. IEEE MILCOM*, 2016, pp. 924–929.
[7] V. C. Chen, *The Micro-Doppler Effect in Radar*. Norwood, MA: Artech House, 2011.
[8] V. Yu. Falileev and R. R. Shatovkin, "Algorithm for recognizing the type of unmanned aerial vehicles by trajectory features," *Vestnik of Russian New University. Series: Complex Systems: Models, Analysis and Control*, no. 3, pp. 34–40, 2020, doi: 10.25586/RNU.V9187.20.03.P.034 (in Russian).
[9] V. A. Bukhalev, *Recognition, Estimation and Control in Systems with Random Jump Structure*. Moscow: Nauka, Fizmatlit, 1996 (in Russian).
[10] I. E. Kazakov, V. M. Artem'ev, and V. A. Bukhalev, *Analysis of Systems with Random Structure*. Moscow: Nauka, Fizmatlit, 1993 (in Russian).
[11] G. A. Ackerson and K. S. Fu, "On state estimation in switching environments," *IEEE Transactions on Automatic Control*, vol. 15, no. 1, pp. 10–17, 1970.
[12] H. A. P. Blom and Y. Bar-Shalom, "The interacting multiple model algorithm for systems with Markovian switching coefficients," *IEEE Transactions on Automatic Control*, vol. 33, no. 8, pp. 780–783, 1988.
[13] Y. Bar-Shalom, X. R. Li, and T. Kirubarajan, *Estimation with Applications to Tracking and Navigation*. New York: Wiley, 2001.
[14] X. R. Li and V. P. Jilkov, "Survey of maneuvering target tracking. Part I: Dynamic models," *IEEE Transactions on Aerospace and Electronic Systems*, vol. 39, no. 4, pp. 1333–1364, 2003.
[15] X. R. Li and V. P. Jilkov, "Survey of maneuvering target tracking. Part V: Multiple-model methods," *IEEE Transactions on Aerospace and Electronic Systems*, vol. 41, no. 4, pp. 1255–1321, 2005.
[16] R. A. Singer, "Estimating optimal tracking filter performance for manned maneuvering targets," *IEEE Transactions on Aerospace and Electronic Systems*, vol. AES-6, no. 4, pp. 473–483, 1970.